Journal of Materials Chemistry A

Accepted Manuscript

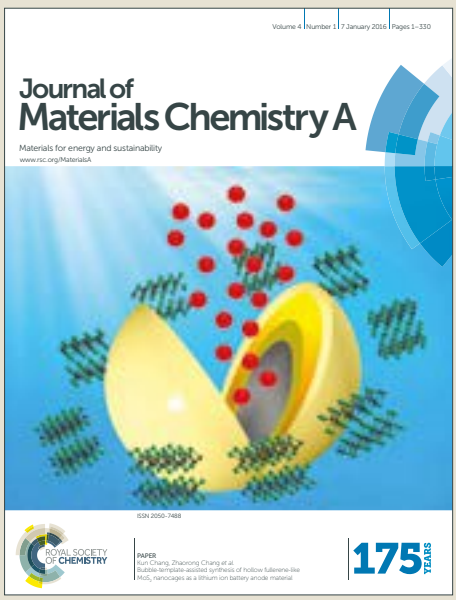

ROYAL SOCIETY OF CHEMISTRY

rsc.li/materials-a

View Article Online
DOI: 10.1039/C9TA04710G

Journal Name

ARTICLE

Achieving High Energy Density and Efficiency Through Integration: Progress in Hybrid Zinc Batteries

Received 00th January 20xx,
Accepted 00th January 20xx

DOI: 10.1039/x0xx00000x

Wenxu Shang[a], Wentao Yu[a], Peng Tan[a*], Bin Chen[b], Zhen Wu[c,d], Haoran Xu[d], Meng Ni[d,e*]

Rechargeable zinc-air batteries, with a high theoretical energy density and intrinsic safety, attract research interests and have great development in recent years. However, hindered by the theoretical potential of 1.65 V, the working voltage is hard to get further increased. In contrast, some conventional Zn-M batteries (M represents transition metal or metal oxide/hydroxide) with low capacities can exhibit high working voltages due to the redox couples with high potentials (e.g., Zn-Ni battery). Thus, combined with Zn-air and Zn-M batteries, hybrid Zn batteries that can achieve both high energy density and efficiency are proposed through using the electrode materials to link these two kinds of reactions. In this report, three types of hybrid Zn batteries (i.e., Zn-Ni/air, Zn-Co/air, and Zn-Ag/air batteries) based on the positive electrode materials are introduced in detail. The positive electrode materials and the achieved electrochemical performance are summarized, and potential applications in electric vehicles and wearable electronics are discussed. Moreover, perspectives on the electrode material optimization, reaction interface design, and operation management are provided. This work gives a timely spotlight on hybrid Zn batteries, and may pave the way for further development of novel electrochemical energy storage systems.

1. Introduction

With the increasing consumption of energy around the world, traditional non-renewable energy sources such as fossil fuels can hardly meet the future demand. It is essential to develop new types of energy, and accordingly, the effective energy storage techniques are in great need. Among them, electrochemical energy storage systems (e.g., supercapacitors and batteries) have attracted great attention.[1–5] As one type of commercialized batteries, lithium-ion batteries (LIBs) are widely applied in consumer electronics and electric vehicles due to the remarkable energy density and efficiency as well as excellent cycling performance.[6–9] However, hindered by the insufficient capacity, high price, and poor safety, the development of next-generation LIBs is still challenging.[10–12]

Among various alternatives to LIBs, rechargeable metal-air batteries (e.g., lithium-air, sodium-air, and zinc-air batteries) have received research interests recently.[13,14] Since one of the reactants, oxygen, is obtained from the ambient air instead of requiring room to store, the theoretical capacities of metal-air batteries solely depend on the metal electrodes, which are much higher than those of LIBs.[15–17] Based on the lightest metal, the lithium-air battery (LAB) has the highest theoretical capacity (3862 Ah kg^{-1}) and energy density (11400 Wh kg^{-1} based on the voltage of 2.96 V). Even considering the whole battery system, it can still deliver the energy density of ~1000 Wh kg^{-1}.[13] Although promising developments have been achieved in recent years, plenty of issues are needed to be solved urgently, such as the low practical capacity, low energy efficiency, and short cycle life.[18] Moreover, the safety issues of LABs are severe owing to the use of metallic lithium and aprotic electrolytes.[19] Conversely, zinc-air batteries (ZABs) become hot research topics currently. This is because first, zinc is more safe, and it can work efficiently in aqueous electrolytes. In addition, ZABs have stronger market competitiveness than LABs owing to the lower prices of zinc and aqueous electrolytes. Moreover, a high energy density of over 1350 Wh kg^{-1} can be delivered based on the theoretical capacity of zinc metal (820 mAh g_{zn}^{-1}) and the potential of 1.65 V.[20,21]

For a conventional ZAB, it contains a metallic zinc electrode (negative electrode), an air electrode (positive electrode), and an aqueous electrolyte, as schematically shown in Fig. 1a. The discharge process includes the oxygen reduction reaction (ORR) occurred on the air electrode and the zinc oxidation to Zn(II) on the metal electrode. During charge, it involves the oxygen evolution reaction (OER) on the air electrode and the Zn(II) reduction on the metal electrode.[22–24] For practical application, ZABs face various issues from the individual structural component to the whole system. For the metal electrode, it is hard to control the irregular dissolution and deposition of zinc, leading to the irreversibility (e.g., dendrite formations, shape changes, and ZnO passivation).[25–27] For the air electrode, the lack of effective bifunctional catalysts results in high overpotentials for both ORR and OER. Additionally, since the

[a] Department of Thermal Science and Energy Engineering, University of Science and Technology of China, Hefei 230026, Anhui, China.
[b] Institute of Deep Earth Sciences and Green Energy, Shenzhen University, Shenzhen, 518060, China.
[c] Shaanxi Key Laboratory of Energy Chemical Process Intensification, School of Chemical Engineering and Technology, Xi'an Jiaotong University, Xi'an, 710049, Shaanxi, China.
[d] Department of Building and Real Estate, The Hong Kong Polytechnic University, Hung Hom, Kowloon, Hong Kong, China.
[e] Environmental Energy Research Group, Research Institute for Sustainable Urban Development (RISUD), The Hong Kong Polytechnic University, Hung Hom, Kowloon, Hong Kong, China.
* Corresponding authors:
Email: pengtan@ustc.edu.cn (Peng Tan)
Email: meng.ni@polyu.edu.hk (Meng Ni)

ORR occurs at a triple-phase (solid electrode, liquid electrolyte, and gaseous oxygen) interface, while the OER at the solid electrode-liquid electrolyte interface requires the release of oxygen timely to prevent the clogging of active surfaces, the inconsistent requirements complex the design of the air electrode structure. Due to the large overpotentials in the ORR and OER, the actual working voltage is usually lower than 1.40 V, while the charge voltage can be higher than 2.0 V, leading to the low energy density and efficiency.[28] In recent years, tremendous efforts have been made on bifunctional electrocatalysts to accelerate the ORR and OER processes.[29–31] For example, Ni_3Fe/N-C sheets have been developed for a ZAB, which delivers a remarkable energy density (634 Wh Kg_{Zn}^{-1}) and great stability (420 h).[32] Cu and Co nanoparticle-co-decorated N-doped graphene nanosheets exhibit a low ORR-OER potential gap of 0.65 V, resulting in a high power density of 170 mW cm^{-2}.[33] However, limited by the theoretical potential of ZABs, to further improve the working voltage is still challenging.[16]

By contrast, although some conventional zinc-based batteries with a closed system (e.g., Zn-Ni, Zn-Mn, and Zn-Ag batteries) have lower capacities than those of ZABs, they can exhibit higher working voltages owing to the redox couples with high potentials (e.g., Ni^{2+}/Ni^{3+}) on the positive electrodes.[34–37] Based on the same negative electrode material (i.e., metallic zinc), a new kind of Zn battery named hybrid Zn battery (HZB) combining Zn-air and Zn-M (M represents transition metal or metal oxide/hydroxide) batteries at the cell level was proposed innovatively by Lee and coworkers.[38] In this way, both the high discharge voltage of a Zn-M battery (>1.7 V) and the high capacity of a Zn-air battery (820 mAh g^{-1}) can be delivered on a single battery. On the positive electrode, the active material in the Zn-M battery can be also used as the catalyst for the oxygen electrocatalysis in the Zn-air battery, linking the electrochemical reactions in two batteries. Consequently, high energy density and efficiency coming from the improved discharge voltage and capacity can be achieved simultaneously.

Focused on HZBs, increasing researches have been made recently, and various types of hybrid Zn batteries have been developed (e.g., Zn-Co/air, Zn-Ag/air batteries).[39,40] Owing to the rapid development of HZBs, the room for exploring novel positive electrodes with excellent electrochemical performance is expanded to some extent. Thus, it is necessary to summarize recent advances in HZBs and provide perspectives for further development. In this work, the configurations and working principles of HZBs are first introduced. Then, based on the positive electrode materials, HZBs are classified into three types (i.e., Zn-Ni/air, Zn-Co/air, and Zn-Ag/air batteries), and the material properties and electrochemical performance are summarized in detail. Furthermore, the battery performance is compared, and potential applications in electric vehicles and wearable electronics are introduced. Lastly, remaining issues on the electrode material optimization, reaction interface design, and operation management are discussed. We hope this work could stimulate the future research of HZBs, and offer references for the design of novel electrochemical energy storage systems with high energy densities and efficiency.

2. Working principles of hybrid Zn-M/air batteries

The schematic illustration of an HZB is shown in Fig. 1b. Similar to that of a ZAB, it consists of a zinc electrode, an aqueous electrolyte, and a positive electrode with active materials.

Take a hybrid Zn-Ni/air battery as an example in which $Ni(OH)_2$ is used as the active material, the electrochemical reactions can be simplified as follows:

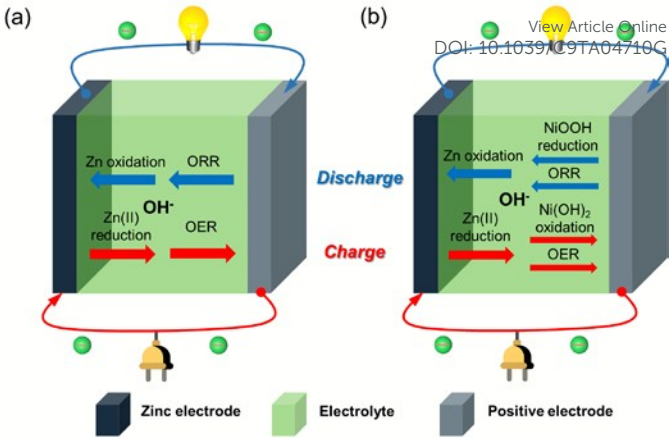

Fig. 1 Schematic illustration of the battery structures and working mechanisms of (a) conventional Zn-air and (b) hybrid Zn-M/air batteries (Take a hybrid Zn-Ni/air battery as an example, and the active material is $Ni(OH)_2$).

Positive electrode:

$$NiOOH + H_2O + e^- \underset{\text{Charge}}{\overset{\text{Discharge}}{\rightleftharpoons}} Ni(OH)_2 + OH^- \quad (1)$$

$$O_2 + 2H_2O + 4e^- \underset{\text{Charge}}{\overset{\text{Discharge}}{\rightleftharpoons}} 4OH^- \quad (2)$$

Negative electrode:

$$Zn + 4OH^- \underset{\text{Charge}}{\overset{\text{Discharge}}{\rightleftharpoons}} Zn(OH)_4^{2-} + 2e^- \quad (3)$$

On the positive electrode, it contains faradaic redox reactions (Eq. 1) and electrocatalytic oxygen reduction/evolution reactions (Eq. 2). During the discharge process, the reduction of the transition metal hydroxide (NiOOH) takes place first, followed by the ORR. During the charge process, the oxidation of $Ni(OH)_2$ and the OER occur in sequence. On the negative electrode, zinc oxidation and Zn (II) reduction occur during discharge and charge, respectively (Eq. 3). The faradaic redox reactions (Eq. 1) can generate reversible pseudocapacitive currents in the narrow potential range, which in turn leads to higher discharge voltages and lower charge voltages than those of ZABs. Meanwhile, the electrocatalytic oxygen reduction reaction (Eq. 2) can provide a high discharge capacity owing to the utilization of oxygen from the ambient air. Therefore, an HZB can exhibit both high energy density and efficiency due to the combination of advantages from Zn-M and Zn-air batteries, outperforming any conventional single Zn-based batteries. This is greatly attractive for a large number of applications that require both high energy and power densities (e.g., electric vehicle), since high voltage can facilitate rapid acceleration and high energy density can improve driving endurance. It is worth noting that although the redox reactions in HZBs have a similar principle (i.e., the change of valence state of transition metal), the detailed reactions are different for different transition metals. For Ni, its final product during charge is NiOOH with the redox reaction of NiO → NiOOH or $Ni(OH)_2$ → NiOOH. For Co and Ag, the final products are the high valence oxides (i.e., CoO_2 and AgO) with the redox reactions of Co_3O_4 → CoOOH → CoO_2 and Ag → Ag_2O → AgO, respectively. For different types of HZBs, the electrode materials and corresponding electrochemical performance will be introduced in detail in the next section.

View Article Online
DOI: 10.1039/C9TA04776C

3. Classification of hybrid Zn-M/air batteries

Based on the active metals, the reported HZBs can be classified into three types (i.e., Zn-Ni/air, Zn-Co/air, and Zn-Ag/air batteries). Assembled with different positive electrode materials with different structures and morphologies, these hybrid Zn batteries show different electrochemical performance, as listed in Table 1. This section will introduce the structures and properties of the electrode materials and the corresponding electrochemical performance.

Table 1 Performance of the hybrid Zn batteries based on different positive electrode materials

Battery type	Positive electrode materials	Loading	Electrolyte	Electrochemical performance						Ref.
				Capacity (mAh g_{zn}^{-1})	Discharge Voltage (V)	Energy density (W h kg^{-1})	Power density	Cycling stability	Energy efficiency	
Zn-Ni/air	$NiO/Ni(OH)_2$ nanoflakes	2 mg cm^{-2}	Gel polymer (with 6 M KOH)	800	1.7→1.1	980	37 mW cm^{-2} @25 mA cm^{-2}	70 cycles at 1 mA cm^{-2} (70 min per cycle)	~80%	38
	$NiO/Ni(OH)_2$-CNT	2 mg cm^{-2}	6 M KOH + 0.2 M zinc acetate	800	1.7→1.2	950	59.1 mW cm^{-2} @42 mA cm^{-2}	192 cycles at 5 mA cm^{-2} (30 min per cycle)	>60%	41
	NiO-Al-Co/carbon cloth	NiO-Al-Co: 1.72 mg cm^{-2}	6 M KOH + 0.1 M zinc acetate	-	1.5→1.14	-	36.3 mW cm^{-2} @71 mA cm^{-2}	1000 cycles at 5 mA cm^{-2} (20 min per cycle)	62%	42
Zn-Co/air	Co_3O_4 nanosheets	2.72 mg cm^{-2}	6 M KOH + 0.02 M zinc acetate	792	1.85→1.0	836	41 mW cm^{-2} @24 mA cm^{-2}	200 cycles at 1 mA cm^{-2} (30 min per cycle)	70%	43
	Co_3O_4 nanowire/Ni foam	3.9 mg cm^{-2}	6 M KOH + 0.1 M zinc acetate	771	1.6→1.05	-	35.7 mW cm^{-2} @68 mA cm^{-2}	1000 cycles at 10 mA cm^{-2} (20 min per cycle)	70%	44
	Co_3O_4/carbon cloth	1.0→4.0 mg cm^{-2}	6 M KOH + 0.02 M zinc acetate	805	-	936	38.6 mW cm^{-2} @25 mA cm^{-2}	400 cycles at 10 mA cm^{-2} (4 min per cycle)	-	39
	Co_3O_{4-x} nanorods	-	6 M KOH + 0.2 M zinc actetate	800	1.90→1.23	1060	3200 W· kg^{-1} @80 mA·cm^{-2}	1500 cycles at 1 mA cm^{-2} (- min per cycle)	>75%	45
	$NiCo_2O_4$/NiF@C	3.4 ± 0.3 mg cm^{-2}	6 M KOH + 0.2 M zinc actetate	688	1.7→1.2	-	26.2 mW cm^{-2} @16.8 mA cm^{-2}	5200 cycles at 5 mA cm^{-2} (30 min per cycle)	~76%	46
	$MnCo_2O_4$/nitrogen -doped reduced graphene oxide	1.2 mg cm^{-2}	6 M KOH + 0.2 M zinc acetate	787	1.7→1.2	813	87 mW cm^{-2} @100 mA cm^{-2}	100 cycles at 1 mA cm^{-2} (40 min per cycle)	~87%	47
Zn-Ag/air	Ag+RuO_2/CNT	Ag: 2 mg cm^{-2} RuO_2/CNT: 2 mg cm^{-2}	6 M KOH + 0.02 M zinc acetate	800	1.85→1.53 →1.25	944	91.9 mW cm^{-2} @157 mA cm^{-2}	100 cycles at 4 mA cm^{-2} (40 min per cycle)	~70%	48
	Ag/Stainless steel	-	6 M KOH + 0.2 M zinc acetate	-	1.8→1.5→1.1	-	-	1700 cycles at 20 mA cm^{-2} (~18 min per cycle)	~60%	49

3.1 Hybrid Zn-Ni/air batteries

Nickel, as one kind of active transition metals, is used in hybrid Zn-Ni/air batteries as the positive electrode material in the form of oxide and/or hydroxide (i.e., NiO and $Ni(OH)_2$). Lee et al. synthesized a $NiO/Ni(OH)_2$ nanoflake composite,[38] in which NiO and $Ni(OH)_2$ demonstrate good electrochemical properties including high pseudocapacitance and excellent oxygen electrocatalytic ability.[49–52] Additionally, NiO can enhance the electrical conductivity of the $NiO/Ni(OH)_2$ composite, leading to the faster charge transfer and higher material utilization.[53] From the scanning electron microscopy (SEM) image of the $NiO/Ni(OH)_2$ composite in Fig. 2a, the nanoflake with the size of ~2 μm presents the highly rippled structure, which makes it tend to separate from each other, creating the interparticle spacing and increasing the active surface areas effectively. While the transmission electron microscopy (TEM) image of an individual $NiO/Ni(OH)_2$ nanoflakes in Fig. 2b exhibits the lattice fringes with spots, demonstrating the crystalline nature, and the selected area electron diffraction (SAED) reveals the polycrystalline property (Fig. 2b, inset). Since the pore can increase the storage room for the electrolyte, the mesoporosity of the

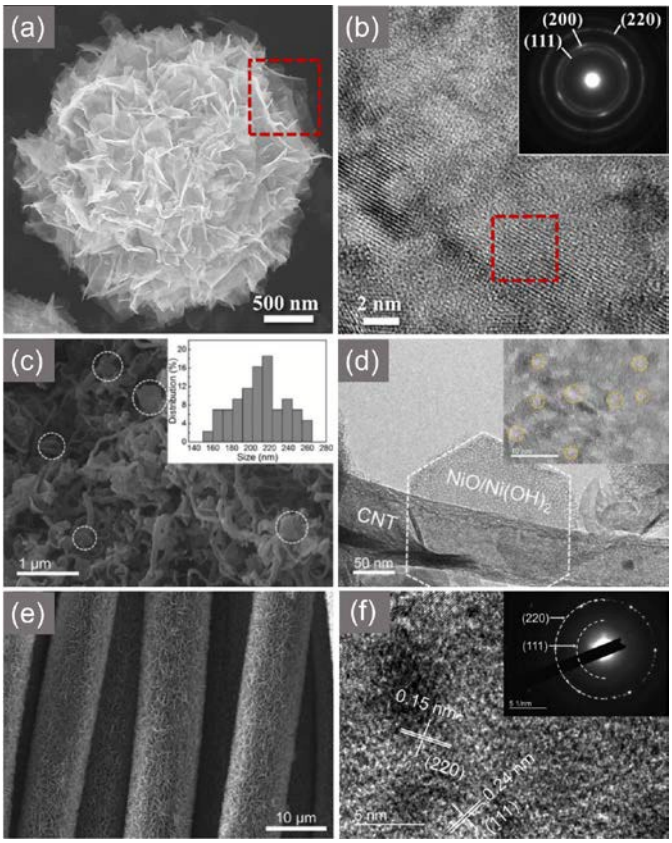

Fig. 2 Characterization of the electrode materials used in hybrid Zn-Ni/air batteries. (a-b) $NiO/Ni(OH)_2$ nanoflakes: (a) SEM image; (b) TEM image with the SAED pattern (inset). Reproduced with permission from ref. 38. Copyright 2016, ACS Publications. (c-d) $NiO/Ni(OH)_2$-CNT: (c) SEM image, the $NiO/Ni(OH)_2$ plates are marked in white circles, and the inset shows the size distribution; (d) Low-resolution TEM image, and the inset shows the generated pores (marked in yellow circles). Reproduced with permission from ref. 41. Copyright 2018, The Electrochemical Society. (e-f) NiO-Al-Co nanosheets on carbon cloth: (e) SEM image; (f) High-magnification TEM image with the SAED pattern (inset). Reproduced with permission from ref. 42. Copyright 2018, Elsevier.

sphere can facilitate the ion transport for faradaic redox reactions. Besides, the morphological features and crystal characteristics lead to the porous property with abundant active sites, promoting the bifunctional oxygen electrocatalytic activity. When assembled it into the battery, two sets of charge and discharge voltage plateaus after galvanodynamic charged and discharged are presented, as shown in Fig. 3a. During charge, it first shows a voltage plateau of ~1.7 V from the oxidation of nickel species (i.e., NiO → NiOOH or $Ni(OH)_2$ → NiOOH), followed by ~2.1 V from the OER. During discharge, it has the voltage plateaus of ~1.7 V from the reduction of nickel species (i.e., NiOOH → NiO or NiOOH → $Ni(OH)_2$) and ~1.1 V from the ORR, respectively. At a high current density of 10 mA cm^{-2}, as illustrated in Fig. 3b, the battery exhibits a discharge voltage of above 1.2 V and a high specific discharge capacity of 800 mAh g^{-1}, which are higher than those of most reported Zn-air battery (<1.2 V for voltage and <600 mAh g^{-1} for capacity).[28] Significantly, both a high energy density of 980 Wh kg_{Zn}^{-1} and a high power density of ~37 mW cm^{-2} can be delivered, demonstrating the successful combination of the advantages from Zn-air and Zn-Ni batteries. Moreover, good cycle stability with the energy efficiency of ~80% after 70 cycles is demonstrated (Figs. 3c, 3d). It is worth noting that benefiting from fast reaction kinetics of nickel redox, the battery shows a remarkable high rate charging capability without any discharge capacity loss. After charging at 9 mA cm^{-2} for 2.4 min, it can work for 22 min at 1 mA cm^{-2} with the same discharge capacity. Even after over 20 cycles, the capacity still remains the same, revealing the great potential for fast charging applications.

Although the hybrid Zn-Ni/air battery with $NiO/Ni(OH)_2$ nanoflakes shows good performance, the electrode material with large sizes is not suitable for fast electron transport, resulting in low utilization of the active surfaces. To tackle this problem and further improve the electrochemical performance, Tan et al. combined the nanoporous $NiO/Ni(OH)_2$ plates with the smaller sizes (~200 nm) and carbon nanotubes (CNTs) to synthesize the $NiO/Ni(OH)_2$-CNT composite.[41] The SEM image of $NiO/Ni(OH)_2$-CNT in Fig. 2c demonstrates that the $NiO/Ni(OH)_2$ plates (marked in white circles) are grown on the CNTs with the average lateral size of only 208 nm, and the TEM image of $NiO/Ni(OH)_2$-CNT in Fig. 2d shows that the $NiO/Ni(OH)_2$ plates can attach on the CNTs in the hexagonal shape. Besides, pores with the size of ~3 nm are formed (marked in yellow circles) as a result of the water release and volume shrinkage during the annealing process. Based on the $NiO/Ni(OH)_2$ plates with small sizes as well as porous structures and CNTs, the $NiO/Ni(OH)_2$-CNT exhibits a high specific surface area of 244.62 m^2 g^{-1} and a large pore volume of 0.476 cm^3 g^{-1}. For the hybrid Zn-Ni/air battery assembled with the $NiO/Ni(OH)_2$-CNT composite, the peak power density reaches 59.1 mW cm^{-2}. Even after 190 cycles at 5 mA cm^{-2}, the battery can still work and maintain the stable charge and discharge voltages of 1.15 and 2.05 V, respectively.[28]

Due to the irreversible phase conversion from α-$Ni(OH)_2$ to thermodynamically stable β-$Ni(OH)_2$ in alkaline solutions over cycles, unfortunately, the hybrid batteries with NiO-based materials suffer from the capacity decrease of the Zn-Ni reaction.[38,41] To improve the stability of α-$Ni(OH)_2$, it is effective to introduce other transition metal ions (e.g., Mn, Al, Co) as dopants.[54–57] Xie et al. reported a cobalt-nickel layered double hydroxide (Co_xNi_{1-x} LDH) electrode doped with the Co ratio of 0.57, which presents excellent stability with the capacity retention of 86.4% after 1000 charge-discharge cycles.[58] Gong et al reported a battery with NiAlCo LDH/CNT as the

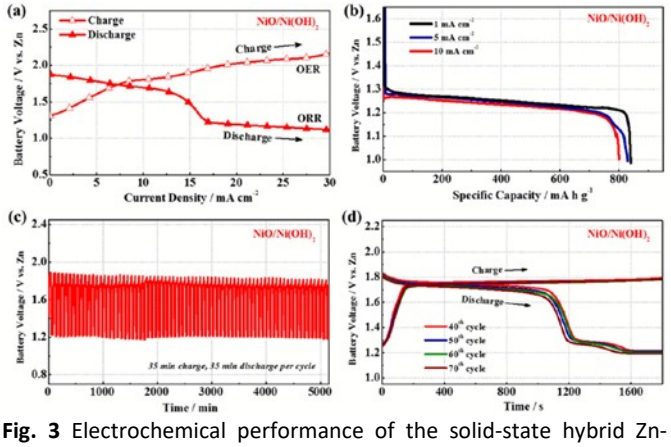

Fig. 3 Electrochemical performance of the solid-state hybrid Zn-Ni/air battery: (a) Galvanodynamic charge and discharge voltages. (b) Full discharge voltage profiles at the current density of 1, 5, and 10 mA cm^{-2}. (c) Galvanostatic charge-discharge cycling profiles at 1 mA cm^{-2} (each cycle contains 35 min charge followed by 35 min discharge). (d) Galvanostatic charge-discharge voltage curves at

40th, 50th, 60th, and 70th cycles. Reprinted with permission from ref. 38. Copyright 2016, ACS Publications.

active material, which exhibits remarkable energy retention of ~94% even after 2000 cycles, revealing the stabilization of α-$Ni(OH)_2$ after Al and Co co-doping.[59] Based on this approach, NiO nanosheets with the co-doping of Al and Co (NiO-Al-Co) on the carbon cloth have been synthesized.[42] From the SEM image of NiO-Al-Co/carbon cloth in Fig. 2e, the nanosheets are grown vertically on the carbon cloth fibers and get entangled to form an interconnected network structure.[60] In addition, since the dopant of Al can suppress the growth of α-$Ni(OH)_2$ and minimize the nanoplate sizes, NiO-Al-Co/carbon cloth has a loose interconnected structure with a large void volume, which facilitates the electron transport and benefits the saturation of electrolyte with the electrode. The TEM image in Fig. 2f shows a well-crystalline structure, and the SAED (Fig. 2f inset) reveals the polycrystalline nature. When served as a positive electrode, the hybrid Zn battery delivers a charge voltage of 1.95 V for the first cycle, even lower than that uses the noble metal catalyst of Ir/C (1.97 V). Moreover, this battery presents the excellent cycle stability with a stable voltage gap of ~65.8 mV and high energy efficiency of ~62% even after 1000 cycles due to the absence of carbon corrosion.[42,61,62]

3.2 Hybrid Zn-Co/air batteries

Cobalt-based materials, especially in the form of cobalt oxides (e.g., CoO and Co_3O_4), have been widely used in metal-air batteries as the electrocatalysts owing to their relatively low prices and excellent activity.[63–66] For example, Zhong et al. synthesized $Co(OH)_2$ and Co_3O_4 nanosheets directly grown on carbon cloth, which exhibited a low overpotential of 0.67 V, a high discharge voltage plateau of 1.18 V at 20 mA cm^{-2}, and excellent stability of ~400 cycles at 5 mA cm^{-2} in a Zn-air battery.[67] Combined with the advantages of Zn-Co and Zn-air batteries, Tan et al. reported a hybrid Zn-Co/air battery made of Co_3O_4 nanosheets grown on carbon cloth as the positive electrode.[43] As demonstrated in Fig. 4a, the SEM image shows the interconnected network intertwined by Co_3O_4 nanosheets, and the TEM image in Fig. 4b reveals the lattice fringes of Co_3O_4 and the SAED pattern. Owing to the direct growth of Co_3O_4 nanosheets on the carbon cloth, this mesoporous structure can enhance the transport of electrons and ions. After assembled into a Zn battery, it demonstrates two sets of voltage plateaus during discharge: one set of ~1.85 V coming from the reduction of cobalt oxides (i.e., CoO_2 → CoOOH → Co_3O_4) and the other of ~1.0 V coming from the ORR. During charge, the voltage plateaus demonstrate the oxidation of Co_3O_4 (i.e., Co_3O_4 → CoOOH → CoO_2) and the OER in the following. Based on the weight of Co_3O_4 and Zn, this hybrid battery delivers an energy density of 846 W h kg^{-1}, much higher than those of the Zn-Co battery (241 W h kg^{-1}).[68] Additionally, the energy efficiency can retain 71% after 200 cycles, revealing good stability.

In addition to the Co_3O_4 nanosheets on carbon cloth, a hybrid Zn-Co/air battery with Co_3O_4 nanowires directly grown on nickel foam (Co_3O_4/Ni foam) has also been reported.[44] The SEM image in Fig. 4a shows the nickel foam covered by uniform Co_3O_4 nanowires. The TEM image in Fig. 4b shows a single nanowire composed of nanoparticles with various pores, which can increase the surface area and facilitate the reaction occurred on the electrolyte-electrode interface. The electrochemical properties of Co_3O_4/Ni foam are given in Fig. 5. In the ORR process, as shown in Fig. 5a, a limiting current density of 25.8 mA cm^{-2} is exhibited at the potential of 0.3 V (vs. RHE), and 82.6% of the initial current density can be maintained after keeping at the potential for 20 h (Fig. 5c). In the OER process, as shown in Fig. 5b, a high current density of 40 mA cm^{-2} is obtained at the potential of 1.58 V (vs. RHE), and the overpotential increases a little (~0.067 V) when maintaining this current density for 20 h (Fig. 5d). The cyclic voltammetry (CV) curves at the scan rate from 1 to 10 mV s^{-1} is given in Fig. 5e to further show the redox properties of Co_3O_4. The lowest scan rate of 1 mV s^{-1} leads to a high capacitance value of 1128 F g^{-1}, and the high capacitance (954 F g^{-1}) can be attained even at a high rate of 10 mV s^{-1}. When assembled in a Zn battery, a power density of ~35.7 mW cm^{-2} and a specific capacity of 771 mAh g_{Zn}^{-1} are delivered. Besides, this hybrid battery can work stably for over 1000 cycles (~333 h).

Since Co_3O_4 has the mixed valence of Co (i.e., Co^{2+} and Co^{3+}), the surface valence can be tuned to enhance the electrochemical performance when served as the positive electrode material.[69–72]

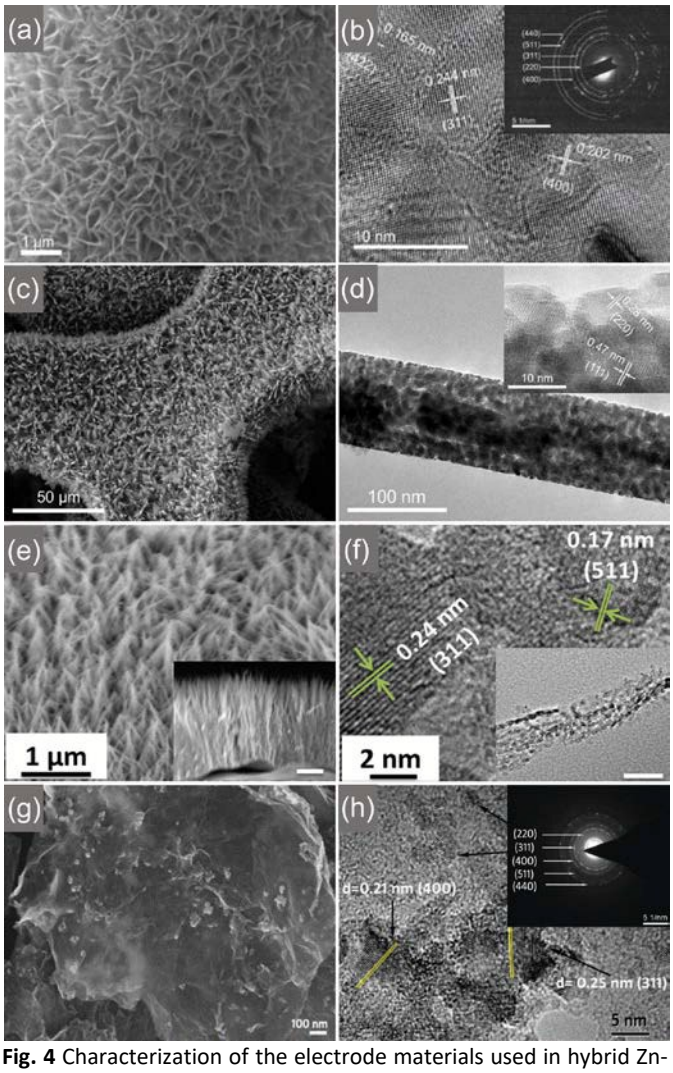

Fig. 4 Characterization of the electrode materials used in hybrid Zn-Co/air batteries. (a-b) Co_3O_4 nanosheets on carbon cloth: (a) SEM image; (b) TEM image with the SAED pattern (inset). Reproduced with permission from ref. 43. Copyright 2018, Wiley Online Library. (c-d) Co_3O_4 nanowires on nickel foam: (c) SEM image; (d) TEM image of one nanowire and the inset shows the high-magnification image. Reproduced with permission from ref. 44. Copyright 2019, Elsevier. (e-f) $NiCo_2O_4$/NiF@C: (e) SEM image with the cross-sectional view of $NiCo_2O_4$ nanowires (inset); (f) TEM with the interconnected nanoparticles on an individual $NiCo_2O_4$ nanowire (inset). Reproduced with permission from ref. 46. Copyright 2017, ACS Publications. (g-h) $MnCo_2O_4$/NGr: (g) SEM image; (h) TEM

image with the SAED pattern (inset). Reproduced with permission from ref. 47. Copyright 2017, Wiley Online Library.

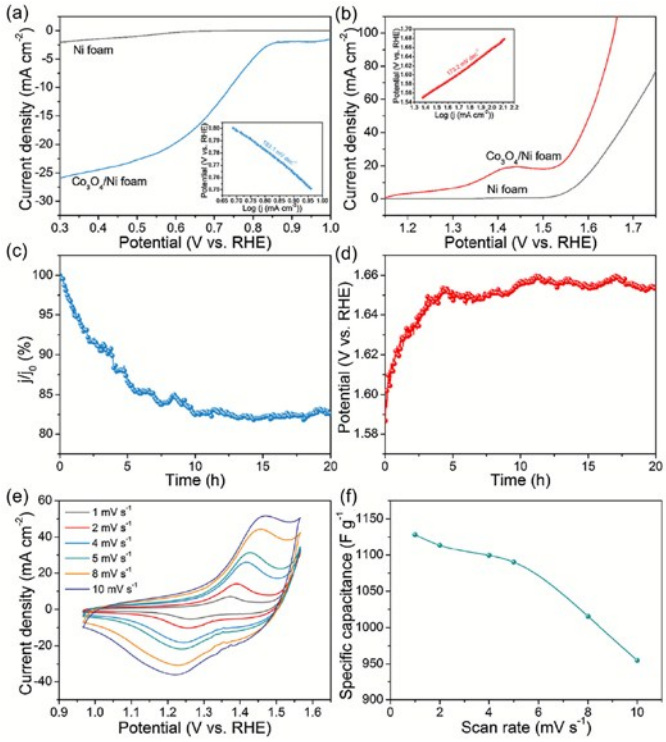

Fig. 5 Electrochemical properties of Co_3O_4/Ni foam in 0.1 M KOH solution: (a-b) LSV curves at the scan rate of 5 mV s^{-1} for (a) ORR and (b) OER, and the insets show the corresponding Tafel plots; (c) ORR chronoamperometric response a constant potential of 0.30 V (vs. RHE); (d) OER chronopotentiometric response at a constant current density of 40 mA cm^{-2}; (e) CV curves at various scan rates; (f) The responding specific capacitance. Reproduced with permission from ref. 44. Copyright 2019, Elsevier.

For instance, Wang et al. reported a Li-O_2 battery with the Co_3O_4 nanosheets electrode tuned by inner oxygen vacancies and the ratios of Co^{2+} and Co^{3+}.[73] It delivers a higher specific capacity of ~24051.2 mAh g^{-1}, better rate performance (8683.3 mAh g^{-1} at 400 mA g^{-1}), and longer cycling life (150 cycles at 400 mA g^{-1}) than the battery with the bulk Co_3O_4. Xu et al. synthesized the Co_3O_4 nanosheets engraved by plasma, which show 10 times higher specific activity than that of the pristine Co_3O_4.[74] For this purpose, a hybrid Zn-Co/air battery based on the Co_3O_{4-x} nanorods engraved by Ar-plasma has been reported by Ma and coworkers.[45] Attributed to the larger surface areas and more oxygen vacancies supplying from Co_3O_{4-x} nanorods, both ORR-OER process and redox reaction of active species are enhanced. Consequently, this hybrid battery demonstrates the high discharge voltage plateaus of 1.90 and 1.23 V, a high power density of 3200 W kg^{-1}, and a significant energy density of 1060 Wh kg^{-1}. Moreover, it empowers remarkable stability of 1500 cycles (440 h) at 5 mA cm^{-2}.

Based on the site preference theory, introducing some other transition metals (e.g., Ni, Mn, and Cu) to Co_3O_4 lattice can get an inverse spinel structure, which can deliver 3D networks of the interconnected interstitial space, facilitating the electrical conductivity and ion diffusivity.[75–79] For example, Shang et al. reported a Zn battery based on the $NiCo_2O_4$ nanowire electrode, which presents an excellent utilization ratio of active material (68.7%),[79] much higher than that of the reported one with the Co_3O_4 electrode (<50%).[64] Considering the excellent electrochemical properties of the active materials after doping, a hybrid Zn-Co/air battery assembled with $NiCo_2O_4$ nanowire electrode has been reported by Li and coworkers.[46] As shown in Fig. 4e, the SEM image of $NiCo_2O_4$ nanowires presents the uniform and dense nanowires directly grown on the carbon-coated nickel foam (NiF@C) surface with the average diameters of ~100 nm and lengths of ~3.5 μm (Fig. 4e inset). The high-resolution TEM image in Fig. 4f reveals a porous structure with abundant interconnected nanoparticles. Benefited from the abundant active sites from the NC-O/NC-O-OH (NC represents Ni or Co) in $NiCo_2O_4$ and remarkable catalytic activity of $NiCo_2O_4$ for both ORR and OER, this battery can empower significant performance. As shown in Fig. 6a, after the initial discharge activation, two charge voltage plateaus are presented, including the oxidation of active species (i.e., NC-O → NC-O-OH) at 1.9 V and the OER at 2.15 V. In the following discharge process, the high voltage of 1.7 V comes from the reduction of active species (i.e., NC-O-OH → NC-O), and the low voltage of 1.2 V comes from the ORR. It is worth noting that even after more than 5000 discharge-charge cycles (over 3 months) at 5 mA cm^{-2}, as shown in Fig. 6b, the battery can still remain the voltage of 1.0 and 2.0 V in the discharge and charge processes, respectively, and the two-step voltage plateaus can still be maintained (Fig. 6c), demonstrating the excellent cycling stability.

In addition to the nickel, the doping of manganese into the spinel structure of Co_3O_4 in the mixed valence states of Mn^{3+} and Mn^{4+} can also improve the catalytic activity, which can be ascribed to the enhancement of C-O-metal and N-O-metal bonding.[81] Besides, embedding the metal or oxides into graphene can further improve the electrochemical performance.[82–84] For instance, Singh et al. synthesized a catalyst composed of Co_3O_4 nanoparticles dispersed on nitrogen-doped reduced graphene oxide (Co_3O_4/NGr) and assembled it into a Zn-air battery, which shows stable discharge voltage profiles at the current densities of 10, 20, and 50 mA cm^{-2}. Moreover, the specific capacity and energy density can reach ~590 mAh g_{Zn}^{-1} and ~840 Wh kg_{Zn}^{-1}, respectively.[85] Using this strategy, Qaseem et al. reported a hybrid Zn-Co/air battery with $MnCo_2O_4$/NGr as the positive electrode material.[47] As indicated in

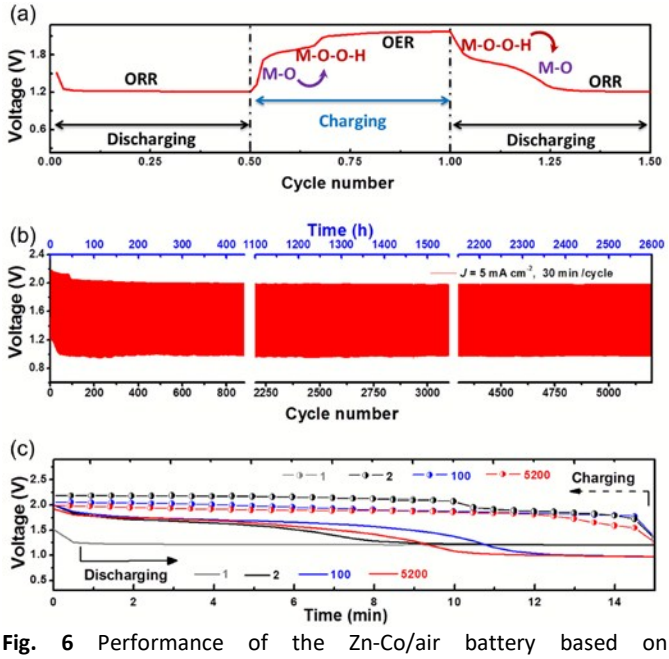

Fig. 6 Performance of the Zn-Co/air battery based on $NiCo_2O_4$/NiF@C: (a) Galvanostatic discharge-charge-discharge curves at 5 mA cm^{-2}; (b) long term cycling stability; (c) Voltage

profiles of the 1st, 2nd, 100th, and 5200th cycles. Reproduced with permission from ref. 46. Copyright 2017, ACS Publications.

Fig. 4g, the SEM image of $MnCo_2O_4$/NGr shows abundant nanoparticles uniformly dispersed on graphene flakes, and the lattice fringes are shown in the TEM image (Fig. 4h). The hybrid battery shows the discharge voltage plateaus of 1.7 and 1.2 V as well as a specific capacity of 787 mAh g_{Zn}^{-1} at the current density of 20 mA cm^{-2}. Benefiting from high catalytic activity and pseudocapacitance of $MnCo_2O_4$/NGr, the higher energy efficiency of 83.7% than that of Pt/C electrode (63.9%) at the current density of 1 mA cm^{-2} is also achieved.

3.3 Hybrid Zn-Ag/air batteries

As one kind of Zn-based batteries, Zn-Ag batteries have been maturely applied in both small and large scales for intrinsic safety and remarkable performance.[86] Apart from Ni- and Co-based electrode metals, Ag can also be used in hybrid Zn batteries as the positive electrode.[48] To compensate for the insufficient OER activity of Ag, RuO_2 nanoparticles on CNT are used as the OER catalyst, through which CNTs can also optimize the distribution of Ag nanoparticles and supply expressway for electron transport.

As illustrated in Fig. 7a, this Zn-Ag/air hybrid battery shows different discharge behaviors at different current densities. At the low current densities (i.e., 2 and 4 mA cm^{-2}), the two charge voltage plateaus of ~1.65 and ~1.95 V correspond to the oxidation of Ag (i.e., Ag → Ag_2O) and the OER, respectively; and the two discharge voltage plateaus of 1.5 and 1.2 V respond to the reduction of Ag (i.e., Ag_2O → Ag) and the ORR. Owing to the addition of RuO_2/CNT with high catalytic activity, the charge voltage is reduced to ~1.95 V in the OER process, which suppress the further conversion of Ag_2O to AgO at high voltages (e.g., >2.0 V). Starting from the current density of 8 mA cm^{-2}, three discharge voltage steps are observed, including the two reduction reactions from AgO to Ag_2O and Ag_2O to Ag at the voltage of ~1.81 and ~1.55 V, respectively, and the ORR at 1.2 V, demonstrating the further oxidation of Ag_2O can be induced in a higher charge voltage.[36] Moreover, at a high current density of 20 mA cm^{-2}, the utilization of Ag can get further enhanced to 70.3%. Compared to the ZABs with state-of-the-art bifunctional catalysts, as shown in Fig. 7b, this hybrid battery shows higher energy efficiency.[87–92] Additionally, after 100 discharge-charge cycles at a high current density of 10 mA cm^{-2} (Fig. 7c), stable charge and discharge voltages of 2.15 and 1.08 V, respectively, can be maintained, and the three discharge voltage steps can be kept with a negligible capacity loss of the Zn-Ag reaction (Fig. 7d), revealing the high cycling stability.

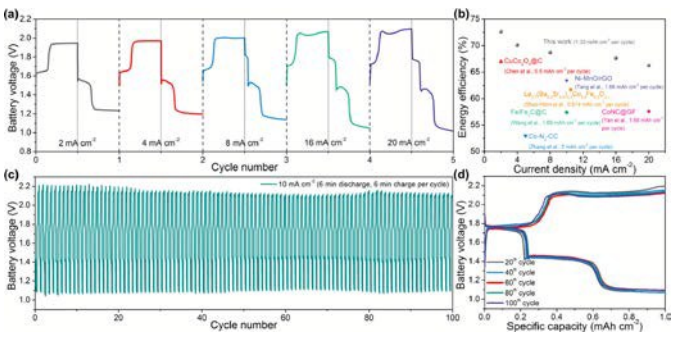

Fig. 7 Rate and cycling performance of the hybrid Zn-Ag/air battery. (a) Charge-discharge voltage profiles at various current densities. (b) Corresponding energy efficiency compared to the reported catalysts. (c) Long-term cycling stability at 10 mA cm^{-2} with a fixed capacity of 1 mAh cm^{-2}. (d) Voltage profiles of the 20th, 40th, 60th, 80th, and 100th cycles. Reprinted from the permission of ref. 48. Copyright 2018, ACS Publications.

Following this work, Chang et al. reported a hybrid Zn-Ag/air battery in which the positive electrode is made of Ag nanoparticles dispersed on the stainless steel screen.[40] Based on this structure, this hybrid battery can remain the stable discharge voltage steps of 1.5 and 1.1 V responding to the reduction of Ag_2O to Ag and the ORR after 1700 cycles at 20 mA cm^{-2} (~551 h), and the coulomic efficiency can still reach 85%.

4. Performance comparisons and applications of hybrid Zn-M/air batteries

The properties of positive electrode materials and the corresponding electrochemical performance of various Zn-M/air batteries are summarized in Table 1. Attributed to the combined advantages of Zn-M and Zn-air batteries, they can exhibit high capacities close to the theoretical value of zinc, high discharge voltages, excellent energy efficiency, and remarkable cycling stability. For Ni, it has only one valence state from Ni^{3+} to Ni^{2+}. For Co, although it can undergo two valence states from Co^{4+} → Co^{3+} → Co^{2+}, the voltages for two reactions are similar in the reported research.[22,93] While for Ag, two distinctive voltages can be demonstrated clearly from Ag^{2+} → Ag^{+} → Ag. Consequently, only one high discharge voltage plateau can be exhibited in Zn-Ni/air and Zn-Co/air batteries, while two can appear in Zn-Ag/air batteries. Moreover, the utilization ratio of the active material is different. Although the electrical conductivity of Ni-based materials can be improved by NiO and/or the addition of CNTs, the intrinsic electrical conductivity of $Ni(OH)_2$ is low. Hence, the maximum utilization ratio in Zn-Ni reaction is still less than 50%.[41] Hindered by high stability of cobalt ions in spinel crystal structure and limited electrical conductivity, Co_3O_4 exhibits the low utilization ratio (e.g., <40%).[68] While for Ag, the utilization is much higher due to the high electrical conductivity of Ag and the introduction of CNTs.[48] Furthermore, the electrocatalytic activity for the ORR and OER is different. For the applied nickel and cobalt oxides or hydroxides with high pseudocapacitance, the ORR activity is insufficient, which leads to low discharge voltages in Zn-air reaction (e.g., only 1.2 V at 5 mA cm^{-2} for Ni and 1.0 V at 5 mA cm^{-2} for Co), while Ag exhibits much higher ORR catalytic activity.[41,43] Conversely, They have effective activity for the OER, which are even better than noble metals, but Ag exhibits poor OER activity, which requires other catalysts to facilitate the charge process.

Owing to the incorporation of fast redox reactions with high potentials, HZBs can offer high power densities. Significantly, a remarkable value (2700 W kg^{-1}) can be achieved at a high current density (60 mA cm^{-2}) when a Zn-Ni/air is galvanodynamic discharged by reversed current density, which can facilitate high power acceleration of electric vehicles.[38] Besides, the hybrid batteries can exhibit a remarkable high rate charging capability

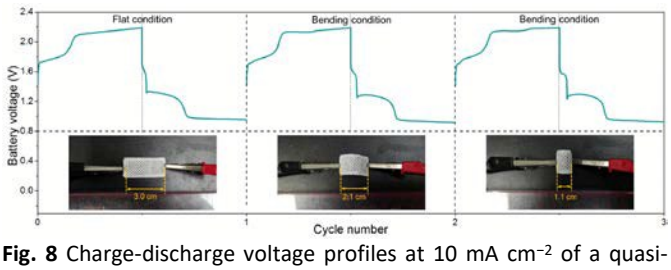

Fig. 8 Charge-discharge voltage profiles at 10 mA cm^{-2} of a quasi-solid-state Zn-Ag/air battery based on the gel electrolyte at

different deformations. Reproduced from the permission of ref. 48. Copyright 2018, ACS Publications.

without any loss of discharge capacity and energy efficiency, which reduce the charging time, promising for future applications (e.g., portable electronics).[43] Moreover, assembled with gel electrolytes instead of aqueous ones, HZBs can also be built as flexible batteries. As depicted in Fig. 8, the quasi-solid-state Zn-Ag/air battery can exhibit a high operating voltage and stable three-step voltage profiles under both flat and bending conditions, manifesting great flexibility, which is promising to apply in wearable electronics (e.g., smart watches).[48]

5. Summary and perspectives

Hindered by the large ORR and OER overpotentials, a conventional ZAB can deliver a high capacity but hardly achieve a high working voltage and energy efficiency. On the contrary, although some Zn-M batteries can offer high working voltages, the capacities are limited by the positive electrode materials. To address these problems, HZBs have been proposed recently. Benefiting from the advantages of Zn-M and Zn-air reactions, both high energy density and efficiency can be achieved simultaneously in a single battery, which is promising for future applications. Although remarkable improvements have been achieved so far, the development of HZBs is still in the early stage. In this work, the working principles and classifications of HZBs have been introduced, and positive electrode materials and the achieved electrochemical performance have been summarized. To realize the commercialization of HZBs, the following issues need to be solved in future research.

First, the electrochemical performance of electrode materials should be further enhanced. The positive electrode materials have to work as the active materials and the electrocatalysts for oxygen electrolysis. Namely, in the redox reactions in the Zn-M reaction region (e.g., Zn-Ni reaction process), they should deliver a high capacity; while in the Zn-air reaction process, they should have high electrocatalytic activity for both ORR and OER. However, the utilization as the active material in the reported HZBs is generally low. For instance, in the hybrid Zn-Ni/air battery, the practical capacity of Zn-Ni reaction is only ~165 mAh g^{-1}, much lower than the theoretical capacity of NiO (360 mAh g^{-1}) or $Ni(OH)_2$ (290 mAh g^{-1});[38] in the hybrid Zn-Co/air battery, the practical capacity for the Zn-Co reaction is 178 mAh g^{-1}, only accounting for 40% of the theoretical value (446 mAh g^{-1});[43] even for the Ag nanoparticles with high electrical conductivity in the Zn-Ag/air battery, the utilization is only around 60%.[43] The low utilization causes the waste of the capacity of active material, decreasing the high discharge voltage region. Besides, the oxygen electrocatalytic activity of the electrode material is insufficient. In the reported HZBs, the voltage plateaus of the ORR are generally lower than 1.2 V, and high charge voltages above 2.0 V are exhibited. Hindered by these issues, HZBs show short high-discharge-voltage regions but high charge voltages, decreasing the energy density and energy efficiency. To further improve the properties of positive electrode materials, many strategies may be applied, including tuning the valence state of transition metal and oxygen, introducing other element ions as dopants, and optimizing the morphology and microstructure.[73,94,95]

Second, the electrode structure should be well designed. Since the active materials are used as both the reactant and the catalyst, the loading in the positive electrode is closely related to the performance. After increasing the loading, more reactant for Zn-M reaction is provided, enhancing the performance. However, a high loading may increase the thickness of the electrode, increasing the oxygen transport resistance, and thus damages the performance of the Zn-air reaction.[24] Additionally, for the air electrodes in ZABs, the triple-phase interfaces are essential for the ORR.[96] While for the Zn-M batteries, the redox reactions of the active materials occur on the two-phase interfaces. Thus, a conflict in the reaction interface exists in HZBs, and a balance between triple- and two-phase interfaces should be established. Thus, to maximize the charge-discharge performance, the loading of active materials and the interfaces of electrodes need optimization.

Third, the electrochemical performance of HZBs with the developed positive electrodes should be comprehensively evaluated. In previous reports, the electrochemical performance of HZBs is usually measured using the methods performed on ZABs. For instance, the voltage-current profile is used to test the power density and the charge-discharge performance; the galvanostatic discharge is used to measure the capacity and energy density; and the pulse charge-discharge cycles at a specific current density and time interval is used to evaluate the energy efficiency and cycling stability.[97] Due to the incorporation of oxidation/reduction o in HZBs, more evaluations should be considered. First, after the battery is charged to different stages, due to the parasitic reactions between the active materials and the electrolyte, the self-discharge may occur, leading to the unwanted loss of charge capacity.[98–102] For HZBs with the half-open systems, when the charged active materials are stored in the air atmosphere, the self-discharge behaviors will be more complicated. In addition, due to the coexistence of the oxidation/reduction of metal oxides and oxygen, the contributions of the two reactions in HZBs is closely related to the discharge depth in the charge-discharge cycles, which can affect the energy efficiency.[48] Moreover, the operating conditions (e.g., temperature and humidity) can affect the performance of ZABs considerably.[28] The impacts of the operating conditions on HZBs, however, has not been reported yet. The missing information will largely affect the proper management for practical applications.

Apart from the above-mentioned materials for HZBs, other transition metal oxides such as MnO_2 may also be served as the positive electrode to link Zn-Mn and Zn-air batteries. While to enable the rechargeability, a near-neutral aqueous electrolyte should be applied,[103] which will be explored in the future. It is worth noting that most research on HZBs focuses on the positive electrode. While the negative electrode, zinc electrode, also has a significant impact on battery performance. For instance, dendrite formation, undesired relocation, and zinc oxide passivation, are closely related to the performance failure. To address these issues, many feasible developments have been reported recently, such as developing porous zinc structure with high surface area, confining zinc in three-dimensional host materials, and direct physical inhibition/suppression.[104] Overall, through the electrode material optimization, reaction interface design, and operation management, a HZB can deliver both high energy density and efficiency, demonstrating great potential for future applications.

Conflicts of interest

There are no conflicts to declare.

Acknowledgments

P. Tan thanks the funding support from CAS Pioneer Hundred Talent s Program and USTC Tang Scholar. Z. Wu thanks the funding support from Hong Kong Scholar Program (XJ2017023) and the China Postd octoral Science Foundation (No. 2016T90913). M. Ni thanks the fun ding support from The Hong Kong Polytechnic University (G-YW2D),

and a grant (Project Number: PolyU 152214/17E) from Research Gr ant Council, University Grants Committee, Hong Kong SAR.

References

1 P. Simon and Y. Gogotsi, *Nat. Mater.*, 2008, **7**, 845–854.
2 S. C. Singhal, *Solid State Ionics*, 2000, **135**, 305–313.
3 C. C. Chan, *Proc. IEEE*, 2007, **95**, 704–718.
4 A. Yoshino, *Angew. Chemie., Int. Ed.*, 2012, **51**, 5798–5800.
5 R. Marom, S. F. Amalraj, N. Leifer, D. Jacob and D. Aurbach, *J. Mater. Chem.*, 2011, **21**, 9938–9954.
6 C. K. Chan, H. Peng, G. Liu, K. McIlwrath, X. F. Zhang, R. A. Huggins and Y. Cui, *Nat. Nanotechnol.*, 2008, **3**, 31–35.
7 C. Wang, H. Wu, Z. Chen, M. T. Mcdowell, Y. Cui and Z. Bao, *Nat. Chem.*, 2013, **5**, 1042–1048.
8 N. Liu, Z. Lu, J. Zhao, M. T. Mcdowell, H. W. Lee, W. Zhao and Y. Cui, *Nat. Nanotechnol.*, 2014, **9**, 187–192.
9 W. Li, Y. Yang, G. Zhang and Y. W. Zhang, *Nano Lett.*, 2015, **15**, 1691–1697.
10 J. Jaguemont, L. Boulon and Y. Dubé, *Appl. Energy*, 2016, **164**, 99–114.
11 L. Lu, X. Han, J. Li, J. Hua and M. Ouyang, *J. Power Sources*, 2013, **226**, 272–288.
12 S. Abada, G. Marlair, A. Lecocq, M. Petit, V. Sauvant-Moynot and F. Huet, *J. Power Sources*, 2016, **306**, 178–192.
13 P. Tan, H. R. Jiang, X. B. Zhu, L. An, C. Y. Jung, M. C. Wu, L. Shi, W. Shyy and T. S. Zhao, *Appl. Energy*, 2017, **204**, 780–806.
14 P. Tan, W. Kong, Z. Shao, M. Liu and M. Ni, *Prog. Energy Combust. Sci.*, 2017, **62**, 155–189.
15 P. Tan, B. Chen, H. Xu, H. Zhang, W. Cai, M. Ni, M. Liu and Z. Shao, *Energy Environ. Sci.*, 2017, **10**, 2056–2080.
16 J. S. Lee, S. T. Kim, R. Cao, N. S. Choi, M. Liu, K. T. Lee and J. Cho, *Adv. Energy Mater.*, 2011, **1**, 34–50.
17 B. Chen, D. Y. C. Leung, J. Xuan and H. Wang, *Appl. Energy*, 2017, **185**, 1303–1308.
18 Y. C. Lu, B. M. Gallant, D. G. Kwabi, J. R. Harding, R. R. Mitchell, M. S. Whittingham and Y. Shao-Horn, *Energy Environ. Sci.*, 2013, **6**, 750–768.
19 D. Geng, N. Ding, T. S. A. Hor, S. W. Chien, Z. Liu, D. Wuu, X. Sun and Y. Zong, *Adv. Energy Mater.*, 2016, **6**, 1–14.
20 G. Toussaint, P. Stevens, L. Akrour, R. Rouget and F. Fourgeot, *ECS Trans.*, 2010, **28**, 25–34.
21 G. Fu, J. Wang, Y. Chen, Y. Liu, Y. Tang, J. B. Goodenough and J. M. Lee, *Adv. Energy Mater.*, 2018, **8**, 1–12.
22 J. Zhang, Z. Xia and L. Dai, *Sci. Adv.*, 2015, **1**, e1500564.
23 E. Lam and J. H. T. Luong, *ACS Catal.*, 2014, **4**, 3393–3410.
24 Z. Wang, D. Xu, J. Xu and X. Zhang, *Chem. Soc. Rev.*, 2014, **43**, 7746–7786.
25 K. Wang, P. Pei, Z. Ma, H. Chen, H. Xu, D. Chen and X. Wang, *J. Mater. Chem. A*, 2015, **3**, 22648–22655.
26 P. Pei, K. Wang and Z. Ma, *Appl. Energy*, 2014, **128**, 315–324.
27 E. M. Bachari, G. Baud, S. Ben Amor and M. Jacquet, *Thin Solid Films*, 1999, **348**, 165–172.
28 Y. Li and H. Dai, *Chem. Soc. Rev.*, 2014, **43**, 5257–5275.
29 G. Fu, X. Jiang, Y. Chen, L. Xu, D. Sun, J. M. Lee and Y. Tang, *NPG Asia Mater.*, 2018, **10**, 618–629.
30 G. Fu, Y. Tang and J. M. Lee, *ChemElectroChem*, 2018, **5**, 1424–1434.
31 G. Fu and J. M. Lee, *J. Mater. Chem. A*, 2019, **7**, 9386–9405.
32 G. Fu, Z. Cui, Y. Chen, Y. Li, Y. Tang and J. B. Goodenough, *Adv. Energy Mater.*, 2017, **7**, 1–8.
33 P. Liu, Y. Hu, X. Liu, T. Wang, P. Xi, S. Xi, D. Gao and J. Wang, *J. Mater. Chem. A*, 2019, **7**, 12851–12858.
34 X. Wang, M. Li, Y. Wang, B. Chen, Y. Zhu and Y. Wu, *J. Mater. Chem. A*, 2015, **3**, 8280–8283. View Article Online DOI: 10.1039/C9TA04710G
35 H. Pan, Y. Shao, P. Yan, Y. Cheng, K. S. Han, Z. Nie, C. Wang, J. Yang, X. Li, P. Bhattacharya, K. T. Mueller and J. Liu, *Nat. Energy*, 2016, **1**, 1–7.
36 D. Ozgit, P. Hiralal and G. A. J. Amaratunga, *ACS Appl. Mater. Interfaces*, 2014, **6**, 20752–20757.
37 R. Kumar, J. Shin, L. Yin, J. M. You, Y. S. Meng and J. Wang, *Adv. Energy Mater.*, 2017, **7**, 1602096.
38 D. U. Lee, J. Fu, M. G. Park, H. Liu, A. Ghorbani Kashkooli and Z. Chen, *Nano Lett.*, 2016, **16**, 1794–1802.
39 P. Tan, B. Chen, H. Xu, W. Cai, W. He and M. Ni, *Electrochim. Acta*, 2018, **283**, 1028–1036.
40 C.-C. Chang, Y.-C. Lee, H.-J. Liao, Y.-T. Kao, J.-Y. An and D.-Y. Wang, *ACS Sustain. Chem. Eng.*, 2018, **7**, 2860–2866.
41 P. Tan, B. Chen, H. Xu, W. Cai, M. Liu, Z. Shao and M. Ni, *J. Electrochem. Soc.*, 2018, **165**, A2119–A2126.
42 P. Tan, B. Chen, H. Xu, W. Cai, W. He and M. Ni, *Electrochim. Acta*, 2018, **290**, 21–29.
43 P. Tan, B. Chen, H. Xu, W. Cai, W. He, M. Liu, Z. Shao and M. Ni, *Small*, 2018, **14**, 1–9.
44 P. Tan, B. Chen, H. Xu, W. Cai, W. He and M. Ni, *Appl. Catal. B Environ.*, 2019, **241**, 104–112.
45 L. Ma, S. Chen, Z. Pei, H. Li, Z. Wang, Z. Liu, Z. Tang, J. A. Zapien and C. Zhi, *ACS Nano*, 2018, **12**, 8597–8605.
46 B. Li, J. Quan, A. Loh, J. Chai, Y. Chen, C. Tan, X. Ge, T. S. A. Hor, Z. Liu, H. Zhang and Y. Zong, *Nano Lett.*, 2017, **17**, 156–163.
47 A. Qaseem, F. Chen, C. Qiu, A. Mahmoudi, X. Wu, X. Wang and R. L. Johnston, *Part. Part. Syst. Charact.*, 2017, **34**, 1–14.
48 P. Tan, B. Chen, H. Xu, W. Cai, W. He, H. Zhang, M. Liu, Z. Shao and M. Ni, *ACS Appl. Mater. Interfaces*, 2018, **10**, 36873–36881.
49 Z. Zhu, J. Ping, X. Huang, J. Hu, Q. Chen, X. Ji and C. E. Banks, *J. Mater. Sci.*, 2012, **47**, 503–507.
50 L. Stern and X. Hu, *Faraday Discuss.*, 2014, **176**, 363–379.
51 J. Liu, C. Guan, C. Zhou, Z. Fan, Q. Ke, G. Zhang, C. Liu and J. Wang, *Adv. Mater.*, 2016, **28**, 8732–8739.
52 S. Yin, Y. Wu, Q. Xiong, H. Qin and H. Zhong, *ChemElectroChem*, 2017, **4**, 2563–2570.
53 M. Wu and H. Hsieh, *Electrochim. Acta*, 2008, **53**, 3427–3435.
54 Y. L. Zhao, J. M. Wang, H. Chen, T. Pan, J. Q. Zhang and C. N. Cao, *Electrochim. Acta*, 2004, **50**, 91–98.
55 W. Hong, T. Zhi-yuan, L. I. U. Yuan-gang and L. E. E. Chang-sheng, *Trans. Nonferrous Met. Soc. China*, 2008, **19**, 170–175.
56 X. Kong, J. Zhao, W. Shi, Y. Zhao, M. Shao, M. Wei, L. Wang and X. Duan, *Electrochim. Acta*, 2012, **80**, 257–263.
57 R. S. Jayashree and P. V. Kamath, *J. Power Sources*, 2002, **107**, 120–124.
58 L. Xie, Z. Hu, C. Lv, G. Sun, J. Wang, Y. Li, H. He, J. Wang and K. Li, *Electrochim. Acta*, 2012, **78**, 205–211.
59 M. Gong, Y. Li, Z. Hongbo, Z. Bo, Z. Wu, F. Ju, H. Wang, Y. Liang, Z. Fan, J. Liu and H. Dai, *Energy Environ. Sci.*, 2014, **7**, 2025–2032.
60 P. Tan, W. Shyy, Z. H. Wei, L. An and T. S. Zhao, *Electrochim. Acta*, 2014, **147**, 1–8.
61 N. Jia Wei Desmond, M. Tang and J. Thomas F., *Energy Environ. Sci.*, 2017, **7**, 2017–2024.
62 C. Ma, N. Xu, J. Qiao and S. Jian, *Int. J. Hydrogen Energy*, 2015, **41**, 9211–9218.
63 X. Chen, B. Liu, C. Zhong, Z. Liu, J. Liu, L. Ma, Y. Deng, X. Han, T. Wu, W. Hu and J. Lu, *Adv. Energy Mater.*, 2017, **7**, 1–11.

64 M. Yu, Z. Wang, C. Hou, Z. Wang, C. Liang, C. Zhao, Y. Tong, X. Lu and S. Yang, *Adv. Mater.*, 2017, **29**, 1602868.
65 J. Liu and X. Sun, *J. Mater. Chem. A*, 2017, **5**, 17804–17810.
66 B. Li, X. Ge, F. W. T. Goh, T. S. A. Hor, D. Geng, G. Du, Z. Liu, J. Zhang, X. Liu and Y. Zong, *Nanoscale*, 2015, **7**, 1830–1838.
67 Z. Song, X. Han, Y. Deng, N. Zhao, W. Hu and C. Zhong, *ACS Appl. Mater. Interfaces*, 2017, **9**, 22694–22703.
68 X. Wang, F. Wang, L. Wang, M. Li, Y. Wang, B. Chen, Y. Zhu, L. Fu, L. Zha, L. Zhang, Y. Wu and W. Huang, *Adv. Mater.*, 2016, **28**, 4904–4911.
69 Y. Wang, T. Zhou, K. Jiang, P. Da, Z. Peng, J. Tang and B. Kong, *Adv. Energy Mater.*, 2014, **4**, 1400696.
70 H. Kim, J. B. Cook, H. Lin, J. S. Ko, S. H. Tolbert, V. Ozolins and B. Dunn, *Nat. Mater.*, 2017, **16**, 454.
71 J. Bao, X. Zhang, B. Fan, J. Zhang, M. Zhou, W. Yang, X. Hu, H. Wang, B. Pan and Y. Xie, *Angew. Chemie., Int. Ed.*, 2015, **54**, 7399–7404.
72 H. Wang, *Chem. Commun.*, 2017, **10**, 2875–2879.
73 J. Wang, R. Gao, D. Zhou, Z. Chen, Z. Wu, G. Schumacher, Z. Hu and X. Liu, *ACS Catal.*, 2017, **7**, 6533–6541.
74 L. Xu, Q. Jiang, Z. Xiao, X. Li, J. Huo, S. Wang and L. Dai, *Angew. Chemie., Int. Ed.*, 2016, **55**, 5277–5281.
75 F. Cheng, J. Shen, B. Peng, Y. Pan, Z. Tao and J. Chen, *Nat. Chem.*, 2010, **3**, 79–84.
76 T. W. Kim, M. A. Woo, M. Regis and K. Choi, *J Phys Chem Lett*, 2014, **5**, 2370−2374.
77 S. Singh, P. Pramanik, S. Sangaraju, A. Mallick, L. Giebeler and S. Thota, *J. Appl. Phys.*, 2017, **121**, 194303.
78 B. Chi, H. Lin and J. Li, *Int. J. Hydrogen Energy*, 2008, **33**, 4763–4768.
79 Z. Yu, L. Chen and S. Yu, *J. Mater. Chem. A*, 2014, **2**, 10889–10894.
80 W. Shang, W. Yu, P. Tan, B. Chen, H. Xu and M. Ni, *J. Power Sources*, 2019, **421**, 6–13.
81 J. Wang, Y. Liang, Y. Li, H. Dai, T. Regier, J. Zhou and H. Wang, *J. Am. Chem. Soc.*, 2012, **134**, 3517–3523.
82 M. Prabu, P. Ramakrishnan, H. Nara, T. Momma, T. Osaka and S. Shanmugam, *ACS Appl. Mater. Interfaces*, 2014, **6**, 16545–16555.
83 M. Prabu, P. Ramakrishnan and S. Shanmugam, *Electrochem. commun.*, 2014, **41**, 59–63.
84 G. Zhang, B. Y. Xia, X. Wang and X. W. Lou, *Adv. Mater.*, 2014, **26**, 2408–2412.
85 S. K. Singh, V. M. Dhavale and S. Kurungot, *ACS Appl. Mater. Interfaces*, 2015, **7**, 21138–21149.
86 J. Wang, X. Wang, W. Kang, C. Yan, C. Y. Foo, M. Cui and P. S. Lee, *Adv. Energy Mater.*, 2013, **4**, 1301396.
87 X. Wang, Y. Li, T. Jin, J. Meng, L. Jiao, M. Zhu and J. Chen, *Nano Lett.*, 2017, **17**, 7989–7994.
88 Q. Wang, Y. Lei, Z. Chen, N. Wu, Y. Wang, B. Wang and Y. Wang, *J. Mater. Chem. A*, 2018, **6**, 516–526.
89 C. Tang, B. Wang, H. F. Wang and Q. Zhang, *Adv. Mater.*, 2017, **29**, 1703185.
90 J.-I. Jung, M. Risch, S. Park and M. G. Kim, *Energy Environ. Sci.*, 2016, **9**, 176–183.
91 X. Sun, T. Qian, C. Yan, M. Wang, N. Xu, S. Liu, J. Liu and Y. Wang, *Adv. Mater.*, 2017, **30**, 1704898.
92 G. Fu, X. Yan, Y. Chen, L. Xu, D. Sun, J. M. Lee and Y. Tang, *Adv. Mater.*, 2018, **30**, 1–10.
93 P. Bhojane, L. Sinha, R. S. Devan and P. M. Shirage, *Nanoscale*, 2017, **10**, 1779–1787.
94 S. Liu, D. Ni, H. F. Li, K. N. Hui, C. Y. Ouyang and S. C. Jun, *J. Mater. Chem. A*, 2018, **6**, 10674–10685
View Article Online
DOI: 10.1039/C9TA04710G
95 M. He, P. Zhang, S. Xu and X. Yan, *ACS Appl. Mater. Interfaces*, 2016, **8**, 23713–23720.
96 J. Ma, L. Jiang, X. Sun, W. Xu, Z. Lu and Y. Li, *Adv. Mater.*, 2016, **28**, 7155–7161.
97 J. Fu, Z. P. Cano, M. G. Park, A. Yu, M. Fowler and Z. Chen, *Adv. Mater.*, 2017, **29**, 1604685.
98 S. Byun, J. Park, W. A. Appiah, M. H. Ryou and Y. M. Lee, *RSC Adv.*, 2017, **7**, 10915–10921.
99 H. A. Andreas, *J. Electrochem. Soc.*, 2015, **162**, A5047–A5053.
100 A. Konarov, D. Gosselink, Y. Zhang, Y. Tian, D. Askhatova and P. Chen, *ECS Electrochem. Lett.*, 2015, **4**, A151–A154.
101 S.-M. Lee, Y.-J. Kim, S.-W. Eom, N.-S. Choi, K.-W. Kim and S.-B. Cho, *J. Power Sources*, 2013, **227**, 177–184.
102 A. Lewandowski, P. Jakobczyk, M. Galinski and M. Biegun, *Phys. Chem. Chem. Phys.*, 2013, **15**, 8692–8699.
103 S. Clark, A. R. Mainar, E. Iruin, L. C. Colmenares, J. A. Blázquez, J. R. Tolchard, A. Latz and B. Horstmann, J. Mater. Chem. A, 2019, **7**, 11387–11399.
104 J. Fu, R. Liang, G. Liu, A. Yu, Z. Bai, L. Yang and Z. Chen, *Adv. Mater.*, 2018, 1805230.

View Article Online
DOI: 10.1039/C9TA04710G

Table of content